DOE/ET-53088-260 IFSR #260

A Split-timestep High-resolution Simulation of 2D Drift-wave Turbulence

Bruce D. Scott

Institute for Fusion Studies
The University of Texas at Austin
Austin, Texas 78712

October 1986

A Split-timestep High-resolution Simulation of 2D Drift-wave Turbulence

Bruce D. Scott

Institute for Fusion Studies, University of Texas, Austin, TX 78712

ABSTRACT

A split-timestep scheme for the simulation of drift-wave turbulence is presented. Large coupling terms in all equations are evaluated at mid-step to avoid severe timestep restrictions. The need for high resolution, not always recognised, is demonstrated. The intermediate scales are kept out of the dissipation range of numerical or artificial diffusion. Coherent structure dynamics at these scales are shown to play an important role in the essential physics of the turbulence. A number of tests of the numerics are presented with the results of a typical run. The numerical methods used here should be useful in most simulations involving large terms which linearly couple separate equations as well as dissipationless intermediate scales.

I. Introduction

Collisional drift-waves have at times been thought to contribute to anomalous transport in fusion devices, particularly particle transport in tokamaks [1]. The essential mechanism is for convective $\mathbf{E} \times \mathbf{B}$ fluctuations driven by the density gradient to combine with density fluctuations in such a way to give rise to a net particle flux down the density gradient [2]. This flux must be several orders of magnitude larger than that predicted strictly from collisional transport if it is to explain the observed transport. The free energy source is the density gradient while magnetic shear damping of the associated outward propagating sound waves acts as the sink [3]. Higher-order effects such as toroidicity [4] or coupling to trapped electrons [5] are necessary for the waves to be unstable. However, it is useful in their absence to study the essential physics of the purely fluid 2D turbulence by considering decaying nonlinear drift-wave turbulence in a slab model with shear.

Previous numerical treatments of drift-wave turbulence have tended to make use of the adiabatic assumption, in which electrostatic and internal energy in the fluctuations are equipartitioned by diffusive processes on a time scale fast compared to that of the waves, yielding a simplifying relation between the density response and the fluctuating electrostatic potential: $n/n_0 = \exp(e\widetilde{\phi}/T)$, or for small fluctuations, $\widetilde{n}/n_0 = e\widetilde{\phi}/T$. This is the relation used in the absence of magnetic shear to get the Hasegawa-Mima equation [6]. It is convenient because the problem is now reduced to one equation, many treatments of which are tractable analytically. To provide for instability, and a cross-field particle flux, a small phase shift, $\delta_{\mathbf{k}}$, is introduced for each wave, so that in wavenumber space one has

$$\frac{\widetilde{n}_{\mathbf{k}}}{n_0} = \frac{e\widetilde{\phi}_{\mathbf{k}}}{T}(1 - i\delta_{\mathbf{k}}), \tag{1}$$

henceforth referred to as the "i-delta" treatment. This relation has been used even when magnetic shear was included and sound-wave resonant damping gives the treatment a second equation [7]. The necessary condition for the adiabatic relation is $\left(\rho_e^2\nu_e, k_\parallel^2 D_\parallel\right) \gg \omega$, where ρ_e is the electron gyroradius, $k_\parallel$ is the component of the wavenumber parallel to the equilibrium magnetic field, and $D_\parallel = T_e/m_e\nu_e$ is the parallel electron diffusion coefficient. Since for all but the smallest tokamaks the perpendicular diffusion rate is slow compared to the diamagnetic frequency, $\omega_* \approx \omega$, the condition becomes $k_\parallel^2 V_e^2 \gg \omega\nu_e$, where V_e is the electron thermal velocity.

The problem with the i-delta treatment now becomes immediately obvious, because in a real system with shear there is always a place where the fundamental mode is resonant, where $k_\parallel$ vanishes. Assuming that $k_\parallel$ is spatially linear near this resonant surface this yields an electron conduction channel, of width $\Delta_D \equiv (\omega_*\nu_e)^{1/2}/k_\parallel' V_e$, in which the fluctuations are hydrodynamic, *i. e.*, the flow fluctuations are decoupled from and not driven by those in the density, although the former can still drive the latter. In this region the linear coupling effects, all of which scale with the parallel gradient, are small, leaving nonlinear turbulent convection to dominate the plasma response to the fluctuating potential. Outside the electron conduction channel the fluctuations are adiabatic: any small phase shift would lead to large parallel currents (see the Ohm's law in the next section). Thus, one is likely to see appreciable particle flux only in the hydrodynamic regions, even if for a single helicity the electron conduction channel is narrow. Clearly, a simple phase relation as in Eq. (1) with constant $\delta_{\mathbf{k}}$'s will fail to represent the correct physics if both regions are present.

What must be done numerically is not only to have separate time-dependent equations for the density and potential, but also to be able to treat spatially varying coupling terms in both equations. Since large shear regions are present, this gives rise to numerical stability problems. A recent treatment with separate density and potential

evolution avoided this by keeping a constant parallel wavenumber, *i. e.*, parallel dissipation was included, but magnetic shear was not [8]. In that case $k_{||}$ is approximated by $k'_{||}\Delta_D$, a value much less than the maximum at the edge of a sheared slab, $k'_{||}x_{\max}$. These terms become very large indeed if many modes are kept. The problem is not so bad if the adiabatic relation is used, for in that case the remaining coupling terms involving ion sound waves are much weaker [7]. Presented here is a numerical method to evaluate such terms implicitly using a split timestep algorithm. The method is useful in any case where large, cancelling terms appear linearly to couple two or more equations together. In the next section the model for 2D drift-wave turbulence is presented. Following this are sections describing the numerical algorithm, important questions of resolution not always addressed, and preliminary results of the simulations.

II. The Model

The basic model for nonlinear drift-wave turbulence in this paper is a 2D sheared slab whose coordinate system of unit vectors $(\hat{\mathbf{x}}, \hat{\mathbf{y}}, \hat{\mathbf{z}})$ is defined respectively by the directions of the density gradient, the fundamental wavevector, $\mathbf{k}_0$, and the magnetic field at the resonant surface, where $k_{||} = k'_{||}x = 0$. The two-fluid Braginskii model [9] is used with the assumptions of electrostatic fluctuations ($\widetilde{\mathbf{B}} = 0$), a thin resonance layer ($k_0\Delta_D \ll 1$), and cold ions ($T_i \ll T_e \equiv T$). The scheme of derivation is the same as that used for nonlinear tearing modes and is explained in detail elsewhere [10]. One then has the Ohm's law and equations for charge conservation, electron continuity, and parallel ion momentum:

$$\eta \widetilde{J}_{\|} = \frac{T}{n_0 e} \nabla_{\|} \widetilde{n} - \nabla_{\|} \widetilde{\phi},$$

$$\frac{d}{dt} \widetilde{\nabla}^2_{\perp} \phi = 4\pi \frac{v_A^2}{c^2} \nabla_{\|} \widetilde{J}_{\|},$$

$$\frac{d\widetilde{n}}{dt} = \frac{1}{e} \nabla_{\|} \widetilde{J}_{\|} - n_0 \nabla_{\|} \widetilde{u}_{\|},$$

$$\frac{d\widetilde{u}_{\|}}{dt} = -\frac{c_s^2}{n_0} \nabla_{\|} \widetilde{n} + \mu_{\|} \nabla^2_{\|} \widetilde{u}_{\|},$$

with the last included to provide for the linear damping mechanism of coupling to outward-propagating ion sound waves. Standard notation is used throughout, with the convective derivative $d/dt \equiv \partial/\partial t + \hat{\mathbf{z}} \cdot (\nabla\phi \times \nabla)$ and the parallel gradient $\nabla_{\|} \equiv (x/L_s)(\partial/\partial y)$, where L_s is the shear length. The tilde refers to the fluctuating variables: the background profiles are held fixed so as to focus on the nonlinear physics. If x, y, and t are respectively scaled by $\rho_s \equiv (M_i/m_e)^{1/2}\rho_e$, k_0^{-1}, and ω_*^{-1}, with $\widetilde{\phi}$, $\widetilde{n}$, and $\widetilde{u}_{\|}$ scaled by $(T/e)(\rho_s/L_n)$, $n_0(\rho_s/L_n)$, and $c_s(\rho_s/L_n)$; we have the dimensionless system of equations used in this paper:

$$\frac{\partial}{\partial t} \nabla^2_{\perp} \phi = -\mathbf{v} \cdot \nabla(\nabla^2_{\perp} \phi) + C^{-1} \nabla^2_{\|}(n - \phi) + D(\nabla^2_{\perp} \phi), \tag{2}$$

$$\frac{\partial n}{\partial t} = -\mathbf{v} \cdot \nabla n - \frac{\partial \phi}{\partial y} + C^{-1} \nabla^2_{\|}(n - \phi) - S \nabla_{\|} u + D(n), \tag{3}$$

$$\frac{\partial u}{\partial t} = -\mathbf{v} \cdot \nabla u - S \nabla_{\|} n + \mu \nabla^2_{\|} u + D(u). \tag{4}$$

where we have dropped the tildes. Here, the second term in Eq. (3) arises from the background density gradient, $\mathbf{v} \cdot \nabla \equiv \hat{\mathbf{z}} \cdot (\nabla\phi \times \nabla)$, $\nabla_{\|} = x(\partial/\partial y)$, and D is a perpendicular operator used solely for numerical purposes to facilitate truncation of the spectrum in $\mathbf{k}$-space. In order to study more clearly the character of conservative transfer in the 2D turbulence, we have not included artificial driving, which would enter in the form of a $\gamma_l \phi_l$ term in the xk_y-space representation of Eq. (3), for each l-th mode. Eqs. (2–4) are evolved within a region of width $2x_L$ about the resonant surface and periodic in y.

The parameters are the ratios $C \equiv (\Delta_D/\rho_s)^2 = (\nu_e/\omega_*)(m_e/M_i)(L_s/L_n)^2$ and $S \equiv L_n/L_s$, with the parallel diffusion coefficient $\mu \equiv \mu_{\|}/\rho_s^2\omega_*$. An additional

parameter is the wavenumber scale $k_0\rho_s$, which appears in the the $\nabla_\perp^2$ operator. The most important of these is C, which determines the electron channel width. In keeping with tokamak ordering S is taken to be small, and then μ is chosen to set the sound wave damping point outside the sound wave resonance point S^{-1} but within the outside limit of computation, where the fields are assumed to vanish. Also, $k_0\rho_s$ is taken to be small, but not infinitesimal, as the essential structure size is expected to be of this order in both the x and y directions. The diffusion coefficient in D is assumed to be sufficiently small that D has no effect at either the largest scales or those at ρ_s sizes.

III. Numerical Algorithm

Upon examination of Eqs. (2–4) it is clear that the most damaging contribution to numerical instability are the $\nabla_\parallel^2$ terms, proportional in xk_y-space to l^2x^2 for the l-th mode, that is, parallel diffusion by electrons must be resolved by the numerical scheme. To see this we consider the simplified system

$$\frac{\partial}{\partial t}\nabla_\perp^2\phi = C^{-1}\nabla_\parallel^2(n-\phi), \tag{5}$$

$$\frac{\partial n}{\partial t} = C^{-1}\nabla_\parallel^2(n-\phi), \tag{6}$$

to isolate the effects of these terms. The linear stability of Eqs. (5,6) is determined for one mode in xk_y-space. We replace $\nabla_\parallel^2$ by $-l^2x^2$, where l is the mode number, and $\nabla_\perp^2$ by $-K^2 \equiv -2g/(\Delta x)^2 - l^2(k_0\rho_s)^2$, where Δx is the step size in the x-direction. The multiplier g may take on values from $\frac{1}{2}\pi^2(\Delta x)^2/x_L^2$ to 2, *i. e.*, we evaluate the finite-differencing in terms of the possible k_x values [11]. A purely explicit scheme with which to evolve Eqs. (5,6) may be expressed as

$$\begin{pmatrix}\phi\\ n\end{pmatrix} = \begin{pmatrix}1-\tau L^2K^{-2} & \tau L^2K^{-2}\\ \tau L^2 & 1-\tau L^2\end{pmatrix}\begin{pmatrix}\phi^0\\ n^0\end{pmatrix},$$

where τ is the timestep, $L^2 \equiv C^{-1}l^2x^2$, and the superscript "0" refers to the previous (backward) timestep. The eigenvalues of the amplification matrix (the 2×2 matrix) must all lie within the unit circle in the complex plane for the scheme to be stable. Evalution of these eigenvalues shows them to take the values unity or $\gamma = 1 - \tau L^2(1 + K^{-2})$. Regardless of the value of K, this scheme will be unstable if the timestep violates the condition

$$\tau < 2L^{-2} = 2Cl^{-2}x^{-2}. \tag{7}$$

This is clearly a catastrophic constraint, since $C^{-1}x_L^2$ is at least 100 (see the next section) and several tens of modes are usually kept.

In contrast to this, the main contributor to the timestep limit in 2D electromagnetic codes is the parallel Alfvén wave, whose equation sets the double time derivative against the $\nabla_\parallel^2$ operator:

$$\frac{\partial^2}{\partial t^2} \leftrightarrow \nabla_\parallel^2,$$

or, upon finite time-differencing,

$$\frac{1}{\tau^2} \leftrightarrow l^2x^2.$$

However, in the case of drift waves there is only one time derivative balancing the parallel diffusion terms: here we have

$$\frac{1}{\tau} \leftrightarrow l^2x^2,$$

an extra factor of lx worse, leading to the timestep constraint given in Eq. (7). In the i-delta treatment the problem does not arise: there are no $\nabla_\parallel^2$ terms because they cancel in the derivation of the Hasegawa-Mima equation [subtracting Eq. (2) from Eq. (3)] [6]. This leaves only the single $\nabla_\parallel$ operator in the sound-wave coupling terms, and these are multiplied by a small coefficient. In the constant-$k_\parallel$ case the balancing is only $\tau^{-1} \leftrightarrow l^2$, easing the present restriction by two orders of magnitude through the

absence of the x^2 contribution [8]. For shear-flow problems with magnetic shear it is a simple matter to evaluate the offending term at the forward time step as it does not couple to another equation. One need only invert the operator

$$\nabla_\perp^2 - \tau l^2 x^2, \tag{8}$$

as a tridiagonal matrix. The tridiagonal is necessary because both the gradient and the spatial dependence enter squared, so that Fourier transforming does not help.

The problem with Eqs. (2–4) is that the $\nabla_\parallel^2$ terms couple two equations. To evaluate them in an implicit manner requires a split timestep in which the homogeneous pieces are handled implicitly in the first half-step, and the inhomogeneous are put in with the second half-step, which also includes inversion of the perpendicular diffusion operators, D. The scheme is necessarily only first-order accurate in the timestep because of the splitting as, for example,

$$\nabla_\perp^2 - \tau D \nabla_\perp^2 - \tau C^{-1} l^2 x^2$$

is replaced by

$$\left(\nabla_\perp^2 - \tau C^{-1} l^2 x^2\right)(1 - \tau D),$$

discarding the piece proportional to τ^2. We illustrate this idea on the system in Eqs. (5,6), without the D operator, to show that the $\nabla_\parallel^2$ terms are stabilised. The finite-differencing is evaluated as before. The first half-step consists simply of inverting the homogeneous pieces, with the rest put in last:

$$\begin{aligned}
\phi^* &= \left(\nabla_\perp^2 - \tau L^2\right)^{-1} \nabla_\perp^2 \phi^0 = \left(1 + \tau L^2 K^{-2}\right)^{-1} \phi^0, \\
n^* &= \left(1 + \tau L^2\right)^{-1} n^0, \\
\phi &= \left(\nabla_\perp^2\right)^{-1} \left(\nabla_\perp^2 \phi^* - \tau L^2 n^*\right) = \phi^* + \tau L^2 K^{-2} n^*, \\
n &= n^* + \tau L^2 \phi^*,
\end{aligned}$$

where the superscript "0" refers to the backward time step and the asterisk to the values at mid-step. This may be expressed in matrix form, after eliminating the mid-step terms, as

$$\begin{pmatrix}\phi\\ n\end{pmatrix} = \begin{pmatrix}\dfrac{1}{1+\tau L^2K^{-2}} & \dfrac{\tau L^2K^{-2}}{1+\tau L^2}\\ \dfrac{\tau L^2}{1+\tau L^2K^{-2}} & \dfrac{1}{1+\tau L^2}\end{pmatrix}\begin{pmatrix}\phi^0\\ n^0\end{pmatrix}.$$

Again ignoring the trivial value of unity, the important eigenvalue of the new amplification matrix is

$$\gamma = \frac{1-\tau^2L^4K^{-2}}{1+\tau L^2\left(1+K^{-2}\right)+\tau^2L^4K^{-2}},$$

which lies within the interval $(-1,1)$ for $\infty > \tau > 0$, regardless of the values of K or L. This part of the overall system is then unconditionally stable, and the overall numerical stability will then be determined by the cascade processes in the nonlinear convective terms, as it is impractical to evaluate these implicitly.

Note that because of the way the density enters Eq. (2) it is necessary to operate on the mid-step ϕ with $\nabla_\perp^2$ before adding in the inhomogeneous term. Finally, the single $\nabla_\parallel$ terms are also evaluated at mid-step, because once the split-step has been formulated it is easy to add in the sound-wave coupling terms with no additional complexity. The total scheme in xk_y-space is then

$$\begin{aligned}
\phi^* &= \left(\nabla_\perp^2 - \tau C^{-1}l^2x^2\right)^{-1}\left[\phi^0 - \tau(\mathbf{v}\cdot\nabla\phi)^0\right],\\
n^* &= \left(1+\tau C^{-1}l^2x^2\right)^{-1}\left[n^0 - \tau(\mathbf{v}\cdot\nabla n)^0 - il\tau\phi^0\right],\\
u^* &= \left(1+\tau\mu l^2x^2\right)^{-1}\left[u^0 - \tau(\mathbf{v}\cdot\nabla u)^0\right],
\end{aligned} \tag{9a}$$

for the first half step, followed by

$$\begin{aligned}
\nabla_\perp^2\phi &= (1-\tau D)^{-1}\left(\nabla_\perp^2\phi^* - \tau C^{-1}l^2x^2n^*\right),\\
n &= (1-\tau D)^{-1}\left(n^* + \tau C^{-1}l^2x^2\phi^* - il\tau Sxu^*\right),\\
u &= (1-\tau D)^{-1}(u^* - il\tau Sxn^*),\\
\phi &= \left(\nabla_\perp^2\right)^{-1}\nabla_\perp^2\phi,
\end{aligned} \tag{9b}$$

for the second. In the first half step, the $\mathbf{v}\cdot\nabla$ terms are evaluated in xy-space, *i. e.*, the code is pseudospectral in y. The problem of aliasing [12] in the convolutions is avoided by restricting the total number of k_y-modes to $\frac{2}{3}N_y$, where N_y is the number of grid points in the y-direction. The number of modes is actually not $\frac{2}{3}N_y$ but half that as a result of the reality condition in which $\phi_{-l}(x)$ is replaced by the complex conjugate of $\phi_l(x)$. Thus, the grid will be $N_x \times N_y$ in real space, or $N_x \times \frac{1}{3}N_y$ in xk_y-space.

Again, because of the x^2 in the first inversion for ϕ the scheme is finite-differenced in the x-direction, as nothing would be gained by transforming to k_xk_y-space, changing the x^2 term into a $\partial^2/\partial k_x^2$ operator. On ther other hand, it may be desirable to do the inversions in the second half step in k_xk_y-space (assuming no spatial dependence in D), especially if the finite-difference approximation to D involves more than three diagonals in the matrix, as is the case if a hyperviscosity is used. In this paper we use the hyperviscosity, so that

$$D = -\mu_\perp \nabla_\perp^4, \tag{10}$$

keeping the dissipation range to the highest k's (see below and the next setion). The second half step proceeds with three transforms, simple division inversions, then four transforms back to xk_y-space. In the present case (drift-wave turbulence) it has been necessary to return to xk_y-space before inverting the $\nabla_\perp^2$ operator as a tridiagonal matrix to avoid difficulty with boundary conditions, which are built-in with the matrix but difficult to handle in k_xk_y-space. This creates additional numerical dissipation which must be lived with because the tendency of the $k\rho_s \sim 1$ modes not to be well localised prohibits the latter approach.

The problem with $x \leftrightarrow k_x$ transforms is that a constant grid spacing must be used. In some cases this has the undesirable effect of forcing high resolution everywhere if it is needed anywhere. One must simply decide whether this disadvantage is

outweighed by the beneficial effects of the hyperviscosity. In the drift-wave case it is, because of the need for a nearly inviscid intermediate range in the spectrum. In any case, the high resolution (see next section) is necessary in the high-shear regions to resolve the accompanying outgoing waves. For the grid size used here the FFT's in the second half step have been seen to take roughly the same computational effort as the tri-diagonal inversions.

The code was initially run with a diffusion operator in xk_y-space of

$$D = \mu_\perp l^4 \nabla_\perp^2, \tag{11}$$

so that xk_y-space needed only be left when doing the pseudospectral convolutions in the nonlinear $\mathbf{v} \cdot \nabla$ operator. This gave a sort of average of k^4, roughly sixth-order in k_y and second order in k_x. However, in shear-flow tests this did not adequately cut off the k_x-spectrum, so the more isotropic hyperviscosity is now used. The limiting form of this is $D \propto k^\infty$, corresponding to a straight truncation in **k**-space with no dissipation. However, the estimation of perpendicular Reynolds numbers for such a truncation becomes problematic for the modes just inside the wall in **k**-space. Also, total Reynolds number estimations like that used by Herring and McWilliams [13] give meaningless values because the dissipation in the modes actually kept is zero. On the other hand, the more physical Newtonian viscosity,

$$D = \mu_\perp \nabla_\perp^2,$$

does not work because the dissipation range in **k**-space is too broad to achieve high perpendicular Reynolds numbers at the intermadiate scales. That is, it is undesirable to have the artificial D operator play much of a role in the physics of the turbulent structures, which in a real plasma are practically inviscid. The hyperviscosity in Eq. (10) was chosen as an adequate compromise, and has been used for similar reasons in the study of coherent structures in decaying Navier-Stokes turbulence [14].

It is possible, but not necessary, to have differing perpendicular diffusion operators in each of the equations. This has been tried in using a smaller "particle diffusion coefficient" [the D in Eq. (3)] than the "perpendicular viscosity", in particular, to set the former to zero. It was found not to be sufficient only to have the artificial diffusion in one or some of the equations, *e. g.*, the neglect of D in Eq. (3) causes problems for the density spectrum even though that for the potential is well-behaved at high l. Since D is artificial, it is simplest to use the same operator in all the equations as this saves space in the computer. One need only be sure that the diffusion is not allowed to play any role in the physics of the turbulence.

The scheme outlined in this section was evolved to handle the problems of 2D drift-wave turbulence, but the split-step method should be useful anytime separate equations are coupled by linear terms which would contribute decisively to numerical instability were they to be evaluated at the backward timestep. If the coupling terms are nonlinear, as in electromagnetic codes where $\nabla_{\|}$ is another convolution operator, such a simple solution as this would not work. A more complicated scheme such as the semi-implicit method used in 3D dynamo simulations [15] would have to be resorted to.

IV. Resolution Considerations

The question of **k**-space resolution in numerical treatments of drift-wave turbulence is very important but often neglected. In particular, there are three space scales in the problem which must be separated. These are the macroscopic gradient scale or experimental system size, represented here by k_0^{-1} or L_n, the most probable structure size, or the intermediate scale here typically on the order of a ρ_s, and the smallest scales at which the numerical or artificial dissipation is acting to truncate the

spectrum. Truncation is neessary because of the finite size of computer core memory, but the cascade process acts to pile energy at the highest k's since there are none higher to which it can be transferred. The operator D serves to remedy this by dissipating the extra energy in lieu of the cascading. However, a real plasma has such a high perpendicular Reynolds number that any important scales are practically inviscid. This is the reason the ρ_s scales must be kept out of the dissipation range of D. Most previous treatments have neglected this consideration [7,8,16], leading to the erroneous conclusion that only the largest scales play important roles in the physics. It is also important to separate the ρ_s scales from the largest to allow any structures which may form to interact on the largest scales. This is well known and has been attended to in previous work [7,8,16].

What is meant here by "perpendicular Reynolds number" is a measure of the relative sizes of the nonlinear coupling term and the artificial diffusion term containing D in a given equation. The real Reynolds number of the entire system will involve a complicated combination of perpendicular and parallel dissipation and the various couplings. Since one looks only for some idea of the scales at which the D terms begin to have importance, the perpendicular Reynolds number is defined as $L^3V/\mu_\perp$ for the hyperviscosity in Eq. (10), where L and V are the scale and characteristic velocity of the particular mode. The length scale enters cubed because of the use of $\nabla_\perp^4$ in Eq. (10). Approximating L by $1/[l(k_0\rho_s)]$ and V by $\omega/[l(k_0\rho_s)]$, all in normalised units where l is the mode number, one arrives at the definition $\left[\mu_\perp(l\times k_0\rho_s)^4\right]^{-1}$ for the perpendicular Reynolds number at the l-th mode, using the diamagnetic frequency for ω. This has been found very useful in locating the dissipation range boundary in k_y-space for the purpose of keeping it away from the important scales. The computations presented in Sec. VI (except for the test of $\mu_\perp$-dependence) were all performed with $\mu_\perp = 10^{-3}$ and $k_0\rho_s = 0.1$, setting the perpendicular Reynolds number to unity at mode 56,

10^3 at mode 10 (also the $k_0\rho_s = 1$ point), and the edge of the dissipation range in the neighborhood of mode 35. The grid resolution is 256×256, which limits the k_y-spectrum to 85 modes so as to automatically avoid the aforementioned aliasing arising from the convolution operations in the nonlinear coupling terms. These smallest scales are highly dissipative under the D operator used. At this size the form of D [either of Eqs. (10,11)] has been seen to have no important effect on the k_y-spectrum up to the dissipation range, which is what is desired. Tests involving the size of D are presented in Sec. VI.

In the x-direction it is important to resolve the smallest of Δ_D and ρ_s with of order 10 points and still keep reasonable separation between all the x-scales in the problem. This is needed in the adiabatic regions as well to resolve the outgoing waves present in the system. The wall at x_L, where the fields are assumed to vanish, must be sufficiently far from the resonance layer that the forced vanishing of all the fields does not reflect outwardly propagating wave energy back into the system. The drift waves couple to ion sound waves near $x = \rho_s L_s/L_n$, the point at which $k_\| c_s$ is equal to the diamagnetic drift frequency. The sound waves then carry energy out and begin to dump it near $x = \mu^{-1/2}$, the point at which the drift frequency is equal to the parallel dissipation rate of the outgoing waves, $\mu_\| k_\|^2$. All of these processes must be well-contained within the walls. This requires in practice that x_L be at least ten or twenty times $C^{1/2}$. Tests have shown 256 points to be the minimum to achieve these conditions. Most previous treatments have avoided this demanding requirement by neglecting magnetic shear, so that an isotropic spectral code may be used [8,16]. The problem, of course, is that the physics of spatially varying shear, present in all real systems, are invisible to such a treatment.

V. Coherence Diagnostics

Before discussing the results and numerical tests of the code, we digress with a few words on coherent structures in the turbulence. These are by definition any recognisable forms in one or more of the fields that persist for a time long compared to the correlation time of the turbulent fluctuations. In a recent study of decaying Navier-Stokes turbulence, coherent vortices were observed to form in an initially Gaussian-randomised fluctuation field and then persist throughout the computations [14], some of which were carried out for tens of correlation times. It is important to use a system of numerical diagnostics in studying these structures due to the fact that the eye is a notoriously poor judge on whether a given distribution is random or not. One such test that is easily implemented is the *kurtosis*, or flatness, defined for zero-mean fluctuations as the ratio of the fourth moment to the square of the second: $\mathrm{Ku}(\phi) \equiv \langle \phi^4 \rangle / \langle \phi^2 \rangle^2$, where the angle brackets represent an ensemble average [17]. For time coherence information the time average is used; for spatial coherence, the averaging becomes an integration over all space. Suitably normalised, this has the value three for a perfectly random, Gaussian distribution. This becomes a very useful diagnostic when the phenomenon under study is not in a stationary state, in which case time correlation measurements are very difficult. A given structure can be followed in successive contour plots, and the kurtosis measurement is used to determine its self-coherence.

Unfortunately, the qualification "suitably normalised" is significant when dealing with localised fluctuations. Clearly, localisation introduces a non-random element into their distribution. Consider for example a case of perfect localisation, *i. e.*, fluctuations $\phi(x, y)$ which are nonzero only within some window $x < x_W$. As long as the averages in the definition of $\mathrm{Ku}(\phi)$ include the entire region $(-x_W, x_W)$, the signal will be proportional to the integration boundary because of the normalisation of the

integrals. In practice, the kurtosis measurement must be compared with that of a fluctuation distribution known to be random-phase. The initial state (see the next section) may be used for this. What one is left with is a rather approximate indication of self-coherence rather than a precise diagnostic. We shall see, however, that the situation will be reasonably clear. The kurtosis measurements in this work were all done with an integration limit of 10.0 in the x-direction, *i. e.*, well outside the region within which the fluctuations are well-confined.

VI. Numerical Tests and Results

The computations are initialised with ϕ and n set equal to each other, and u set to $Sx\phi$, a natural form suggested by Eq. (4). The initial field for ϕ is an isotropic, random-phase Gaussian realisation with a spectrum given by $E_{\mathbf{k}} \propto k/\left[1+(k\rho_s)^4\right]$, multiplied by a spatial gaussian envelope to reflect localisation to the resonant surface due to magnetic shear, then normalised so that the rms velocity fluctuation is unity, *i. e.*, marginally nonlinear. A picture of this distribution is shown in Fig. 1. It has a measured kurtosis of $\mathrm{Ku}(\phi) = 11$, which is used as a benchmark for these measurements. The fluctuations are not expected to remain adiabatic for long, as the density gradient and nonlinear couplings act to force n and ϕ apart, but this is a reasonable initial state because the most dangerous terms in Eqs. (2–4) cancel initially, allowing the fields to find the appropriate time-dependent solution with minimal violence. Coherent structures are not assumed at the beginning but may form as the fields evolve. This initial state is then advanced according to the algorithm in Eqs. (9a,b).

The typical run consists of a rapid transient phase in which the fluctuations adjust to a state in which the nonadiabatic piece of the density response, h, has risen from zero and then become confined within the electron conduction channel, and then

a long decay phase characterised by the dominance of a few large coherent structures in h. The basic features of one such run are depicted in Fig. 2. This was carried out with $C = 1.0$, $S = 0.2$, $k_0\rho_s = 0.1$, $\mu = 0.02$, $x_L = 20.0$, $\mu_\perp = 10^{-3}$, and the timestep $\tau = 10^{-3}$. In a), b), and c) are shown the fluctuation contours in ϕ, n, and h, respectively, at $t = 8.0$. This is during an intermediate decay phase, lasting until $t \approx 10.0$, in which turbulence characteristics measurements like kurtosis are relatively stationary. The zero contour is suppressed for clarity. The most obvious property is the general localisation to the vicinity of the resonant surface. This is the strongest for h, as electron parallel diffusion strongly damps this quantity outside the electron conduction channel. Localisation in n and ϕ is due to overall magnetic shear damping. The structure in h is also much more complicated than that in either n or ϕ. This is borne out by the kurtosis measurements, which yield $\mathrm{Ku}(h) = 36$, while $\mathrm{Ku}(\phi) = 8$ and $\mathrm{Ku}(n) = 12$ (that of the randomised initial state is 11). More important than the absolute values is the fact that the kurtosis in h is a factor of 3 or so higher than that in either n or ϕ. Besides the obvious self-coherence, this indicates that the character of h is so different from the other fields that a simple phase relation between n and ϕ like that in Eq. (1) cannot suffice. The actual relation is highly spatially dependent, as is clear from the adiabaticity of the fluctuations in the high-shear regions. This demonstrates the need for a way to correctly and completely handle the $\nabla_\parallel^2$ terms in Eqs. (2–4), as they will be present in any drift-wave system consisting of both high- and low-shear regions.

The importance of the intermediate scales is shown by the second half of Fig. 2, in which the spectra of ϕ, n, and h appear in d), e), and f), respectively. Superimposed upon the mid range background are pronounced maxima in the region $k_y\rho_s \gtrsim 1$. The strength of the largest scale reflects the combination of the smaller structures into larger ones. The latter feature is most evident in h, as the coherent

structures there are the most dominant. This is where the necessity of high resolution and low dissipation enters, for if either were relaxed these phenomena would not be correctly reproduced. The roles of the intermediate scales would be missed and the conclusion that the largest scales are the only important ones would be reached.

The first test applied to this system was to check the behaviour at the boundary as a function of x_L. This is a rather severe test because of the constraints on the cross-field scales discussed in Sec. IV. The problem is localisation of the outgoing sound waves to which the drift waves are coupled. Several runs with the same randomised initial state were carried out with x_L values of 5.0, 10.0, and 30.0. These were done only long enough to see clear differences at the boundary. Such a situation was achieved at $t = 4.0$. At this time the results of all but the largest value (30.0) of x_L were compared. Shown in Fig. 3 are cuts of the total energy, defined by

$$E_T(x) \equiv \sum_{l=1}^{N} \left(|\nabla_\perp \phi_l(x)|^2 + |n_l(x)|^2 + |u_l(x)|^2 \right),$$

where N is the number of modes. The ideal case is for the cut to be flat at zero in the neighborhood of $x = x_L$. Clearly seen is that $x_L = 5.0$ is too narrow a region to contain the waves. The case of $x_L = 10.0$ looks adequate on this cut, but mode profiles show that while the largest and smallest scales are well-confined, the intermediate scale $k_y \rho_s \sim 1$ is not. The main run ($x_L = 20.0$) shows good behaviour not only on this cut but also in all the mode profiles. Expanded views of these profiles verify that the inner regions are still well-resolved.

With the smallest value of x_L thus eliminated, the other runs were continued up to $t = 8.0$. A comparison was done on the total energy decay rate, defined as $\gamma \equiv E_T^{-1}(\partial E_T/\partial t)$. Shown in Fig. 4 are the decay curves for all four runs, labelled with markers according to the value of x_L used. The transient state is shown only for the largest value. Also note that the run with the smallest value was terminated at

$t = 4.0$. The important point is that there is rough convergence between the middle values, even though the intermediate scales (comprising some tenths of the total energy) behave badly for $x_L = 10.0$. The largest value is clearly bad, for near the end of the run the decay rate becomes a growth rate. For this value the resolution in the interior is insufficient and the run becomes unstable. Thus, a proper convergence check is not really possible due to the fact that only one run is well-behaved throughout. It is this test that determines $x_L = 20.0$ to be the usual value for $C = 1$.

To test the numerics the fields at $t = 8.0$ were pulled from the above run and used in initial conditions for short runs in which τ and $\mu_\perp$ were varied. A convergence test on the timestep was first performed. The fluctuations at $t = 8.0$ were started in four runs with τ's of 10^{-2}, 3×10^{-3}, 10^{-3}, and 3×10^{-4}, each carried for about two ω_*^{-1}-times. The spectra of h at the end of these runs are shown in Fig. 5, superposed upon one another. The spectra are labelled with markers corresponding as shown to the above timesteps. They are in good agreement at all scales except for the high-l failure for $\tau = 10^{-2}$. Time dependent phenomena do not come out so well, as seen in the evolution curves for the total energy decay rate, which appear in Fig. 6, labelled as in the previous figure. As the timestep becomes larger, accuracy problems in tracking the cascade processes become more pronounced until the algorithm enters a nonlinear numerical instability regime, probably caused by terms of the form $(\partial/\partial x)D_{nl}(\partial\phi_l/\partial x)$, where D_{nl} is a nonlinear diffusion coefficient dependent on the field amplitudes. If the study is confined to the characteristics of the turbulence, *i. e.*, spectra and structures, the present first-order accurate scheme suffices, but close investigation of properties like decay rates will require second-order accuracy in the timestep.

The next test involved the same set-up as for the timestep test except that the parameter varied was $\mu_\perp$, which took the six values 10^{-2}, 3×10^{-3}, $10^{-3} \ldots 3 \times 10^{-5}$. The spectra of h for each of these runs are compared in Fig. 7, which uses the same

labelling scheme as in Fig. 5. As expected, most of the difference is at the highest mode numbers. For $l \lesssim 20$, *i. e.*, the region including the intermediate peak as well as the largest scales, the runs are remarkably convergent. For the smallest value of $\mu_\perp$ the high l's are not sufficiently damped, and the run would eventually become unstable due to pile-up of energy in that part of k_y-space. The reason that $\mu_\perp$ is not set higher than 10^{-3} is seen in Fig. 8, in which the total energy decay rates for the different $\mu_\perp$ values are compared. After the initial adjustment period, the decay rate becomes independent of $\mu_\perp$ for $\mu_\perp > 10^{-3}$. Thus, the artificial diffusion does not have great effect at these values and thus does not interfere with interpretation of the results.

VII. Discussion

A split-timestep scheme for managing the problems which may come in high-resolution spectral simulations of turbulence has been presented. The linear coupling terms which become large for the highest modes are stabilised by the numerical scheme which evaluates them in an implicit manner. This carries the advantages of implicit algorithms without resorting to the inversion of very large sparse matrices, which would be needed because of the coupling between equations. As in all implicit methods, however, this scheme adds timestep-dependent dissipation to the simulation, so that time-dependent phenomena such as decay rates would necessitate the improved accuracy that a second-order scheme would provide. This could be achieved with the use of an additional corrector step, with the drawback of increased effort per timestep, but such a procedure should not more than double this effort [15]. The present first-order accurate scheme does in any case accurately represent the basic characteristics of drift-wave turbulence such as spectra, coherence properties, and spatial correlations. It should be useful in making other problems tractable as well.

Acknowledgments

The author would like to thank Dr. J.-N. LeBoeuf for extensive discussions of numerical problems in shear-flow simulations that had much bearing on the algorithm presented here, Dr. P. H. Diamond for consultations on the roles of coherent structures and turbulent statistics, and Drs. LeBoeuf and P. W. Terry for helpful criticism of the manuscript. This work was supported by the U. S. Department of Energy, Contract No. DEFG0580ET53088.

References

[1] P. Liewer, *Nucl. Fusion* **25**, 543 (1985).

[2] P. W. Terry and P. H. Diamond, *Phys. Fluids* **28**, 1419 (1985).

[3] L. D. Pearlstein and H. L. Berk, *Phys. Rev. Lett.* **23**, 220 (1969).

[4] Liu Chen and C. Z. Cheng, *Phys. Fluids* **23**, 2249 (1980).

[5] C. S. Liu, Marshall N. Rosenbluth, and W. M. Tang, *Phys. Fluids* **19**, 1040 (1976).

[6] A. Hasegawa and K. Mima, *Phys. Rev. Lett.* **39**, 205 (1977).

[7] D. Biskamp, *Phys. Lett.* **109A**, 34 (1985).

[8] M. Wakatani and A. Hasegawa, *Phys. Fluids* **27**, 611 (1984).

[9] S. I. Braginskii, in *Reviews of Plasma Physics*, edited by M. A. Leontovich (Consultants Bureau, N. Y., 1965), Vol. 1, p. 205.

[10] Bruce D. Scott, Ph. D. Dissertation, University of Maryland, Physics Publ. # 85-186, 1985.

[11] R. D. Richtmeyer and K. W. Morton, *Difference Methods for Initial-value Problems*, 2nd ed. (Interscience, New York 1967).

[12] David Gottlieb and Steven A. Orszag, *Numerical Analysis of Spectral Methods: Theory and Applications*, CBMS-NSF Regional Conference Series in Applied Mathematics, Vol. 26 (SIAM, Philadelphia 1977).

[13] J. R. Herring and J. C. McWilliams, *J. Fluid Mech.* **153**, 259 (1984).

[14] J. C. McWilliams, *J. Fluid Mech.* **146**, 21 (1984).

[15] Douglas S. Harned and D. D. Schnack, *J. Comp. Phys.* **65**, 57 (1986); D. S. Harned and W. Kerner, *J. Comp. Phys.* **60**, 62 (1985).

[16] R. E. Waltz, *Phys. Fluids* **26**, 169 (1983).

[17] A good discussion of moments as applied to drift-wave turbulence can be found in P. W. Terry, Ph. D. Dissertation, University of Texas, 1981.

Figure Captions

Fig. 1. Contours showing the form of the initial fluctuation distribution $\phi(x, y)$. Solid contours indicate positive values; dotted, negative. The interval is linear. The spectrum is peaked at mode 10. $\mathrm{Ku}(\phi) = 11$.

Fig. 2. Contours (as in previous figure) and spectra of a typical run. Note the scale expansion for clarity in the h contours. Angle brackets reflect an integration over x. l is the mode number. Snapshot at $t = 8.0$, when $\mathrm{Ku}(h) = 36$.

Fig. 3. Cuts of the total energy, $E_T(x)$, for different values of x_L. These runs started at $t = 0$ from the randomised initial condition normally used.

Fig. 4. Decay rate (γ) curves comparing the four runs with different x_L values. Individual curves are labelled with the marker shown according to the value used.

Fig. 5. Effect on the energy spectrum of h of varying the timestep. Individual spectra are labelled with the marker shown according to the value of τ used. l is the mode number.

Fig. 6. The same runs as in Fig. 5, comparing the decay rates, γ. This is an illustration of the effects of first-order accuracy.

Fig. 7. Effect on the energy spectrum of h of varying the artificial diffusion. Individual spectra are labelled with the marker shown according to the value of $\mu_\perp$ used.

Fig. 8. The same runs as in Fig. 7, comparing the decay rates, γ. Convergence is achieved after the adjustment period for $\mu_\perp \lesssim 10^{-3}$.

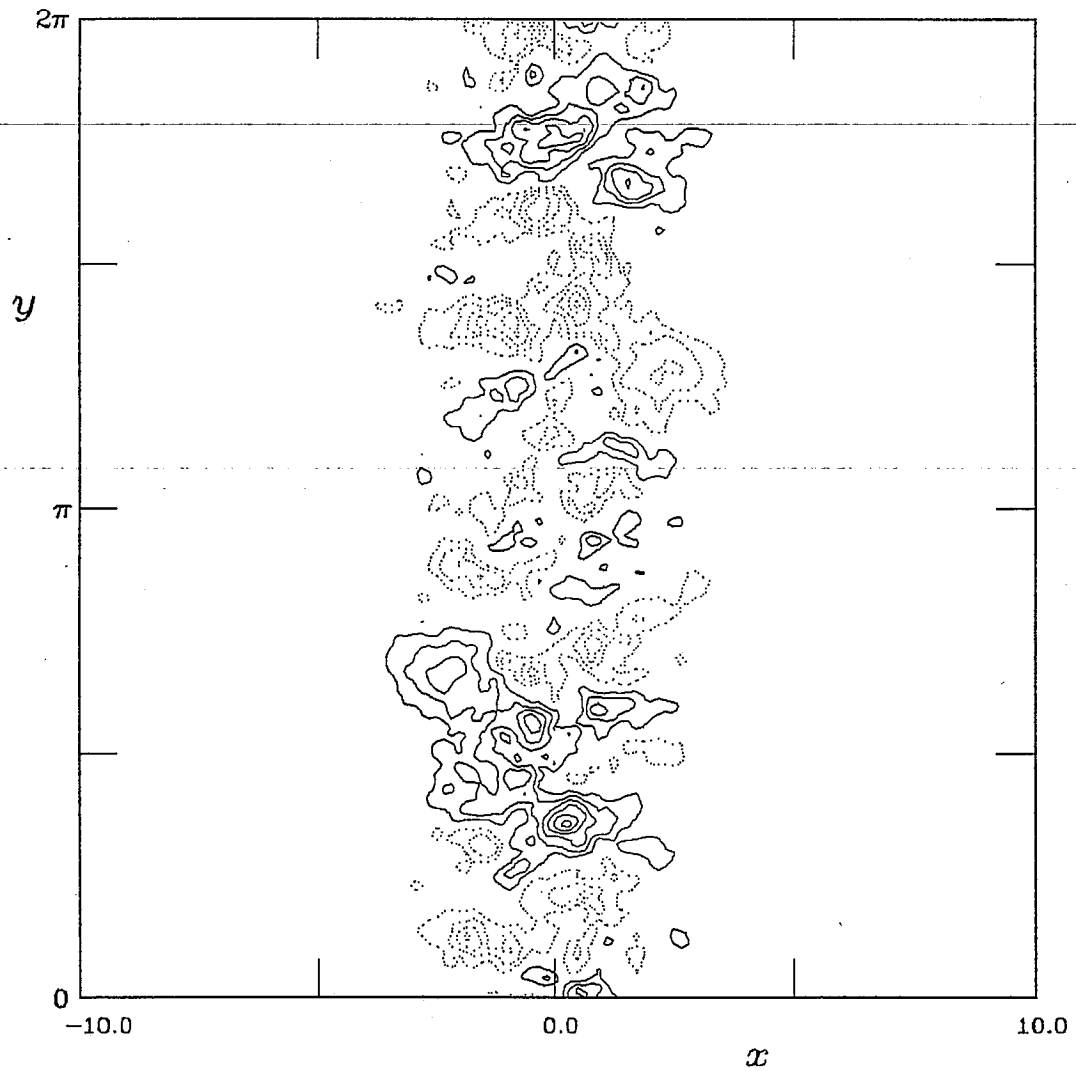

Fig. 1.

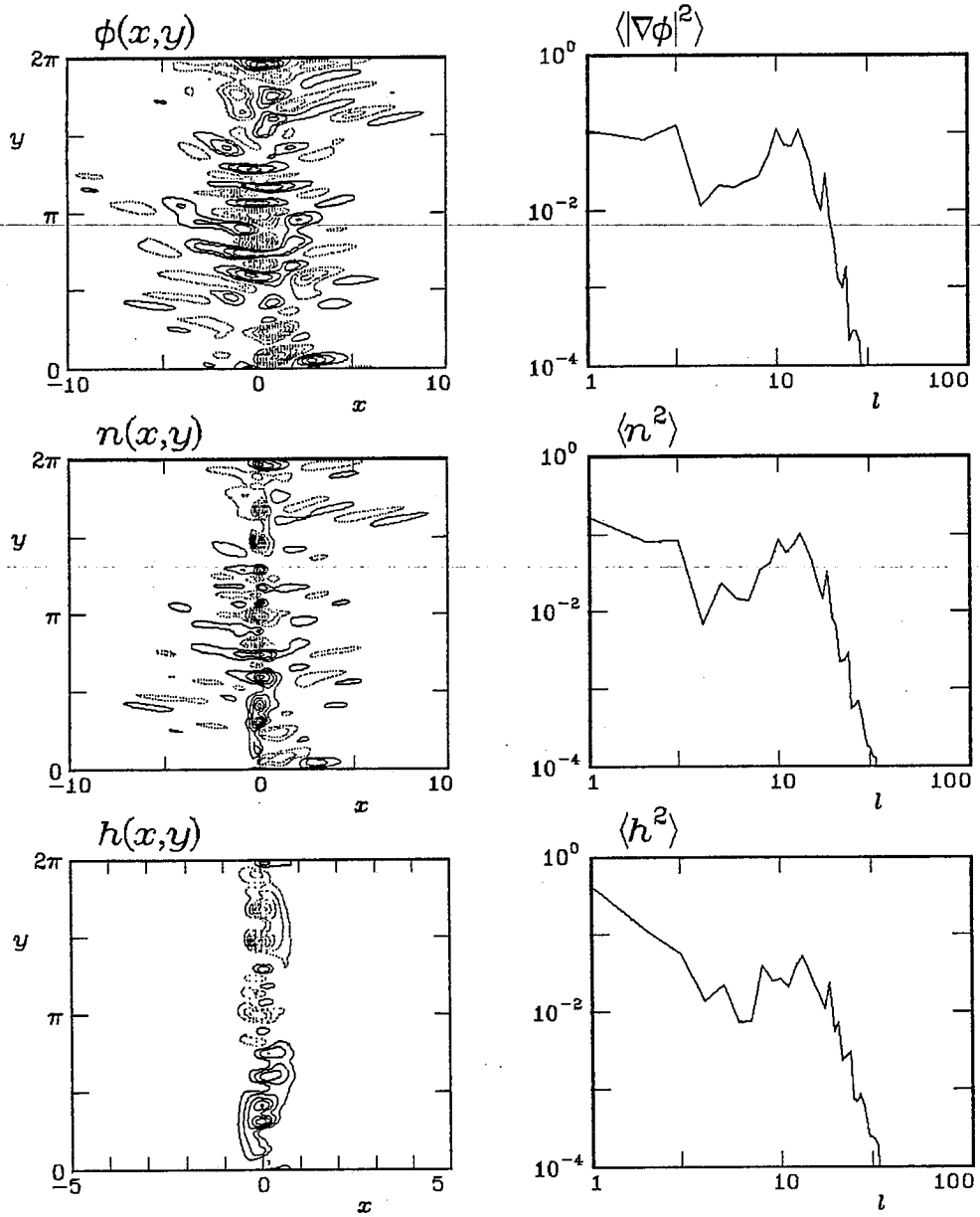
$\phi(x,y)$
$\langle|\nabla\phi|^2\rangle$
$n(x,y)$
$\langle n^2\rangle$
$h(x,y)$
$\langle h^2\rangle$
2π
π
0
y
x
l
10^0
10^{-2}
10^{-4}
1
10
100
−10
−5
5

Fig. 2.

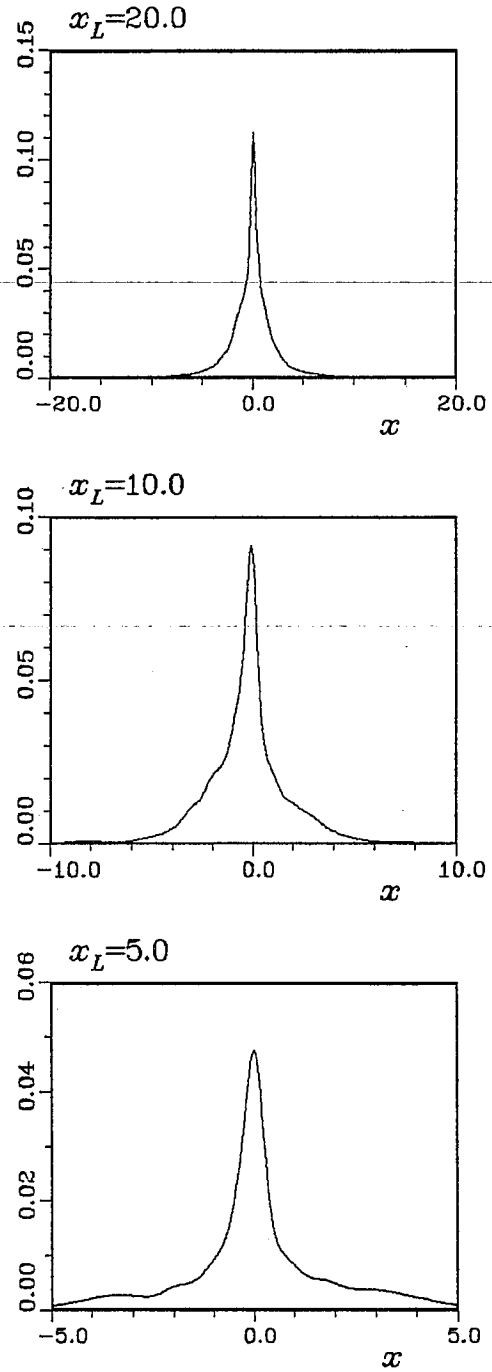
x_L=20.0
0.15
0.10
0.05
0.00
−20.0
0.0
20.0
x
x_L=10.0
0.10
0.05
0.00
−10.0
0.0
10.0
x
x_L=5.0
0.06
0.04
0.02
0.00
−5.0
0.0
5.0
x

Fig. 3.

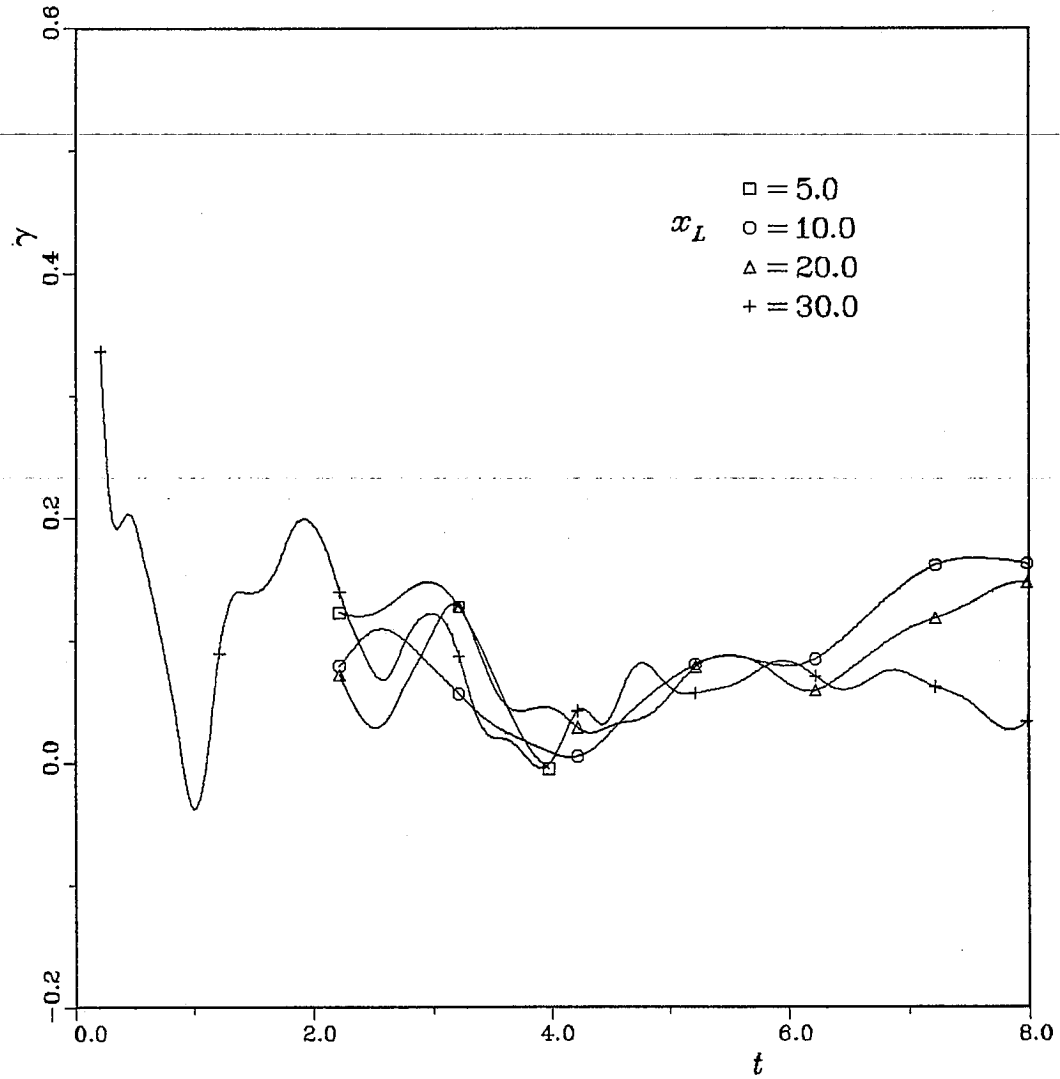

Fig. 4.

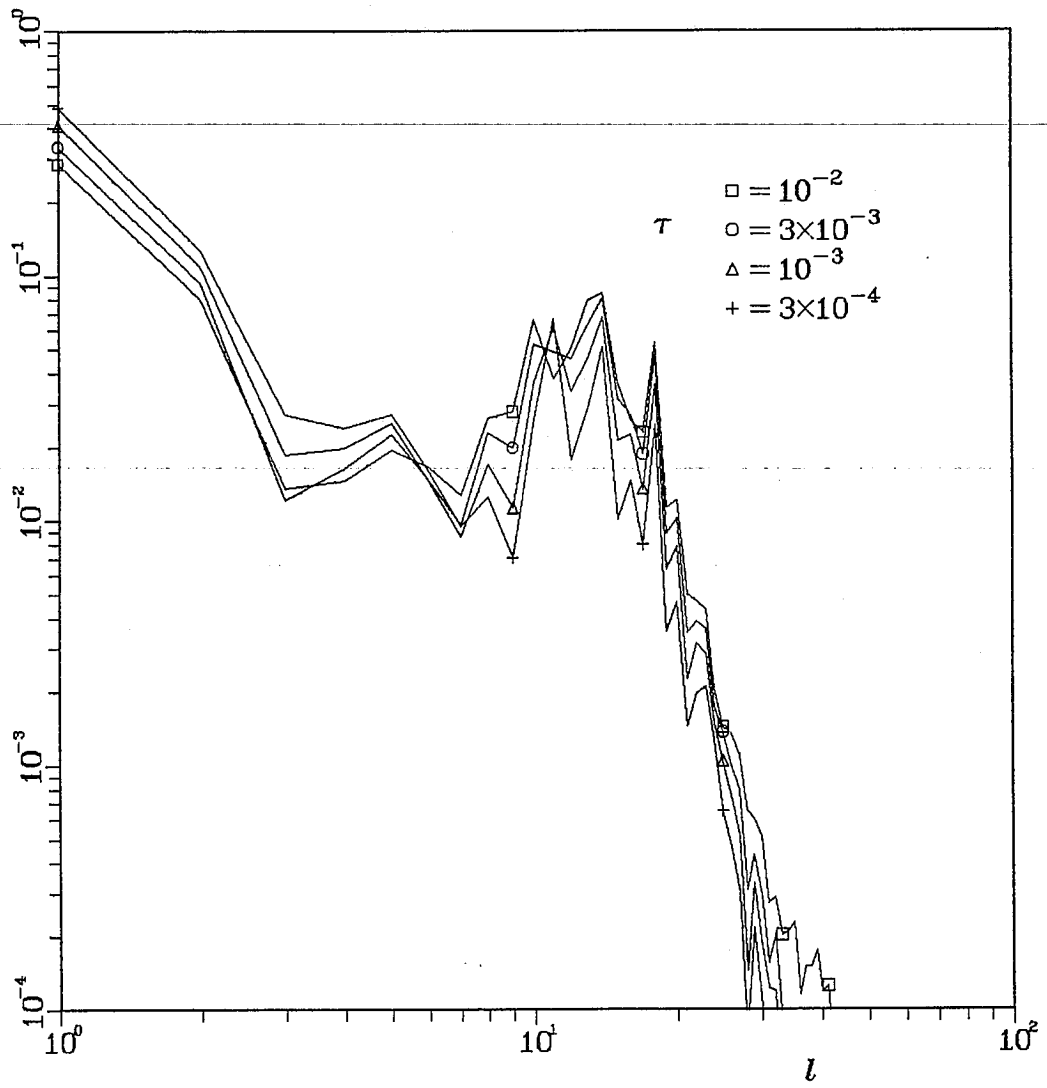
10^0
10^{-1}
10^{-2}
10^{-3}
10^{-4}
10^0
10^1
10^2
l
τ
$\square = 10^{-2}$
$\circ = 3\times10^{-3}$
$\triangle = 10^{-3}$
$+ = 3\times10^{-4}$

Fig. 5.

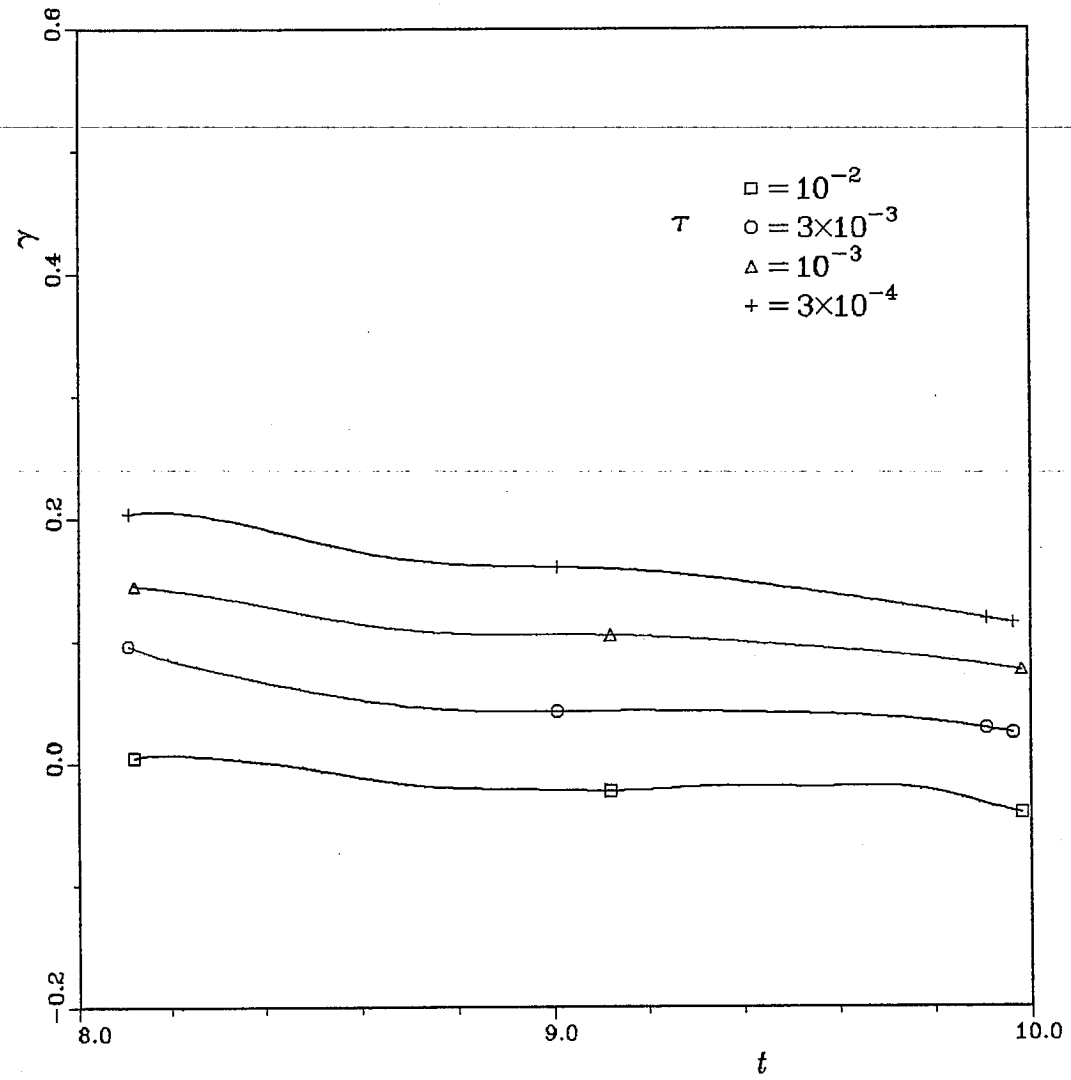

Fig. 6.

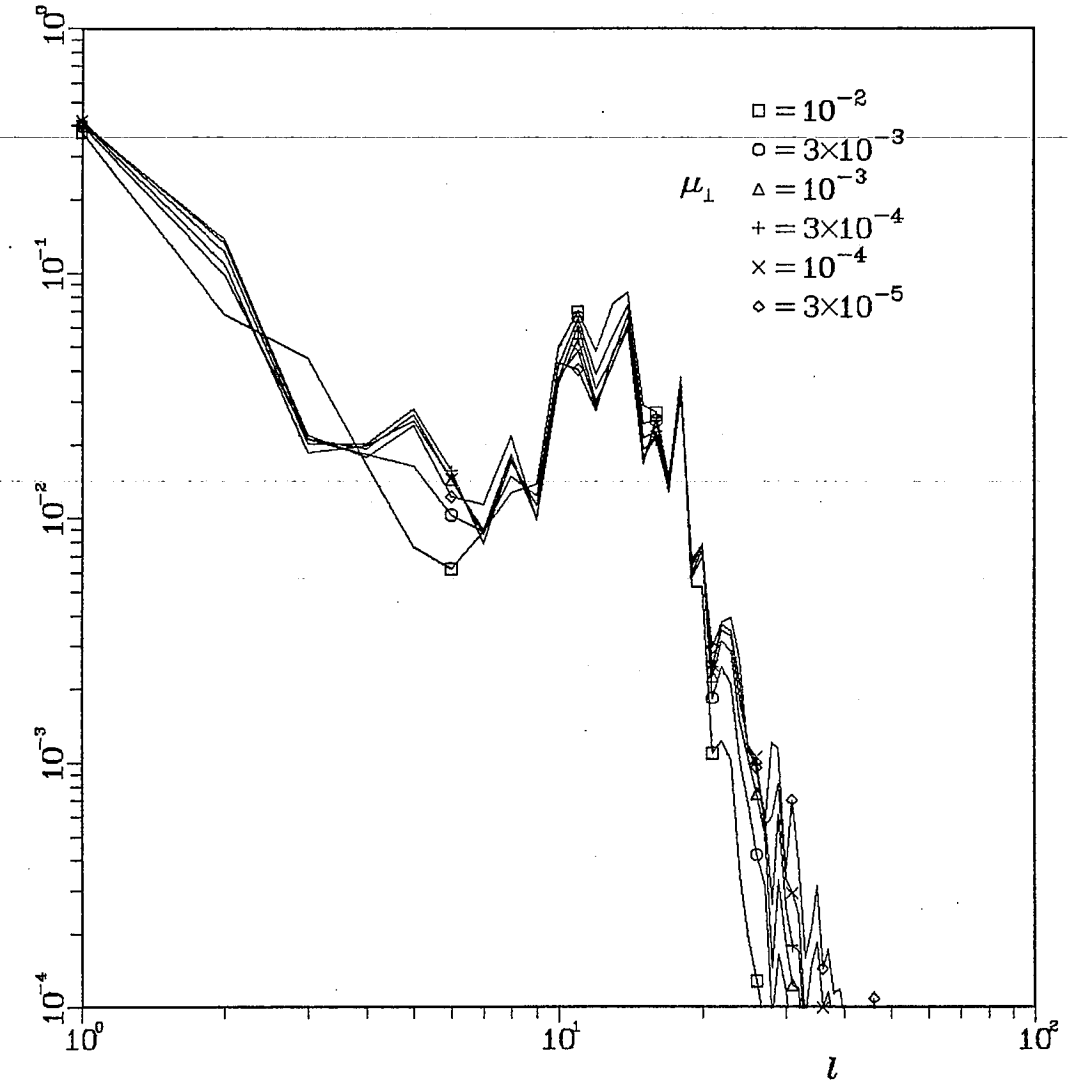
10^0
10^{-1}
10^{-2}
10^{-3}
10^{-4}
10^0
10^1
10^2
l
$\mu_\perp$
□ = 10^{-2}
○ = 3×10^{-3}
△ = 10^{-3}
+ = 3×10^{-4}
× = 10^{-4}
◇ = 3×10^{-5}

Fig. 7.

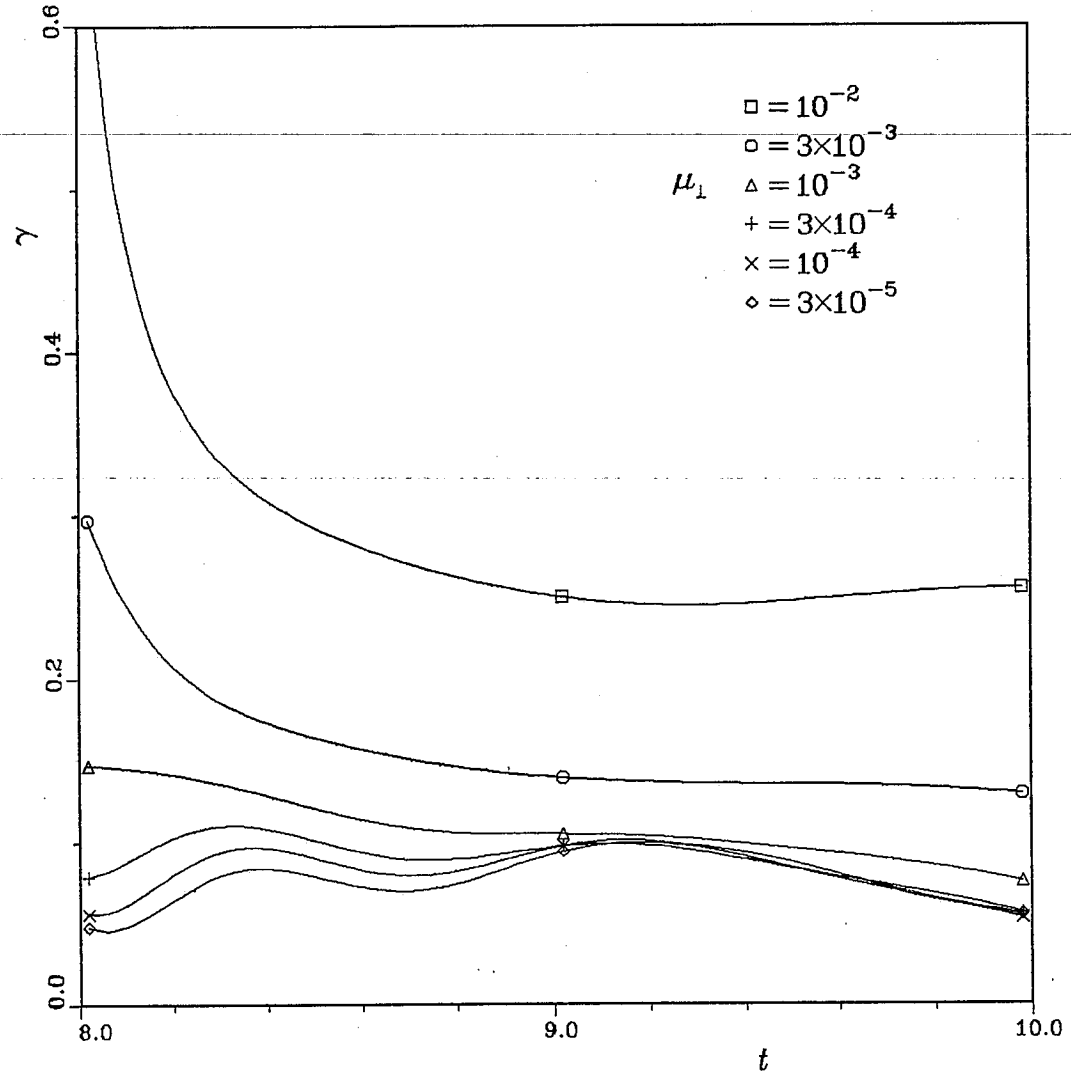

Fig. 8.